Supplementary Information

Metallic 2D Janus SNbSe Layers Driven by a Structural Phase Change

*Cheng-Lun Wu[1], Mohammad Y. Sayyad[1], Renee E. Sailus[1], Dibyendu Dey[2,5], Jing Xie[3], Patrick Hays[1], Jan Kopaczek[1,4], Yunbo Ou[1], Sandhya Susarla[1], Ivan S. Esqueda[3], Antia S. Botana[2], Seth A. Tongay[1,]**

[1]Materials Science and Engineering, School for Engineering of Matter, Transport and Energy, Arizona State University, Tempe, Arizona 85287, USA

[2]Department of Physics, Arizona State University, Arizona 85287, USA

[3]Electrical Computer and Energy Engineering, Arizona State University, Arizona 85287, USA

[4]Department of Semiconductor Materials Engineering, Faculty of Fundamental Problems of Technology, Wroclaw University of Science and Technology, Wybrzeże Wyspiańskiego 27, 50-370 Wrocław, Poland

[5] Department of Physics and Nanotechnology, SRM Institute of Science and Technology, Kattankulathur, Tamilnadu 603203, India

Heat of formation calculation

Monolayers	Phase	H_f (eV/atom)
NbS_2	1H	-1.053
	1T	-1.021
$NbSe_2$	1H	-0.859
	1T	-0.826
SNbSe	1H	-0.958
	1T	-0.921

Table S1 Heat of formation (H_f) of NbS_2, $NbSe_2$ and SNbSe monolayers in their respective 1H and 1T phases. As shown, the 1H phase is energetically slightly more favorable in all cases, with a difference of ~30 meV, which is comparable to the thermal energy (~25 meV) at room temperature. This small energy difference suggests that these monolayers can be experimentally synthesized in either phase.[1]

Vacancy formation energy calculation

Monolayers	Phase	E_v (eV/atom)
NbS_2	1H	1.618
	1T	1.167
$NbSe_2$	1H	1.601
	1T	0.603

Table S2 Vacancy formation energy (E_v) of NbS_2, $NbSe_2$ monolayers in their respective 1H and 1T phases. The calculated E_v describes qualitatively that, in both H and T phases, it is possible to create chalcogen vacancies, which are crucial for the SEAR process and chalcogen replacement. Since the E_v is lower in the 1T phase in both material systems, creating vacancies and substituting them with other chalcogens to form a Janus monolayer is comparatively easier than in the 1H phase. However, in this study, we focused on 1H-phase NbS_2 and $NbSe_2$ as the starting material for Janus conversion, with the SEAR process parameters adjusted for etching the top chalcogen layers.

SEAR Janus conversion comparison

The Janus conversion process parameters for Nb-based TMDs inherently differ from those for W- and Mo-based TMDs. Due to the variations in bond dissociation energies, the RF power required to generate H_2 plasma with sufficient energy to create chalcogen vacancies also varies. Therefore, TMDs with stronger in-plane covalent bonds would require more RF power for bond dissociation. These disparities are also observed when comparing the conversion for sulfide- and selenide-based TMDs. The difference in dissociation energy can be attributed to the variations in electronegativity and atomic size between transition metal and chalcogen atoms. In the results, the energy required to create a sulfur vacancy (V_S) is greater than that of a selenium vacancy (V_{Se}), when considering sulfur-transition metal (S-M) and selenium-transition metal (Se-M) covalent bonds.[2] With sufficient plasma energy to initiate the conversion process, a steady supply of H_2S (H_2Se) is crucial for the continuation of chalcogen replacement rather than only etching the original chalcogen atoms. Finally, allowing sufficient conversion time is important to achieve full Janus conversion of the TMD. Additionally, in-situ monitoring of the Raman mode evolution during SEAR conversion is a powerful way to assess the conversion progress, which was employed during the conversion process of SWSe and SMoSe.[2] However, Nb-based metallic TMDs exhibit laser-induced oxidation during the prolonged in-situ monitoring process, as well as exhibiting weak Raman signal and interference with hydrogen plasma, which prevent for utilizing Raman spectroscopy during the SEAR process.

Our studies indicate that SEAR conversion of CVD-grown monolayer NbS_2 to SNbSe requires RF power of 90 W for a duration of 10 minutes, whereas mechanically exfoliated monolayer $NbSe_2$ to SeNbS requires only 5 W for 10 minutes. For comparison, conversion for CVD-grown WSe_2 to SeWS using a similar ICP setup requires 15 W for 18 minutes, while CVD-grown $MoSe_2$ to SeMoS requires 15 W for 8 minutes.[3] Notably, a higher RF power was required for Janus conversion of an S-based TMD compared to a Se-based TMD. This is caused by the shorter and stronger metal-sulfur bond compared to the metal-selenium bond, requiring more energetic plasma to create sulfur vacancy sites compared to selenium vacancy sites.[2] When comparing the conversion process amongst only the Se-based TMDs, $NbSe_2$ required less RF power than $MoSe_2$ and WSe_2, and this is due to the relatively weaker Nb-Se bond. These differences highlight the nuanced energy landscape of the SEAR conversion process, which is influenced by both the chalcogen-metal bond and the transition metal species.

As described in the two previous paragraphs, the synthesis process differs between SeNbS and SNbSe based on the starting material. Although in both cases, the constituents of the synthesized Janus structure are the same, their order can vary depending on the synthesis process; in SNbSe, it is sulfur-niobium-selenium atomic stacking from top to bottom, whereas in SeNbS, it is selenium-niobium-sulfur stacking from top to bottom. As a result, the structural differences lead to the formation of opposite electric fields and the build-up of strain. This is related to the different electronegativity and atomic size of chalcogen atoms. Moreover, in the case of SNbSe, the electric field is downward oriented, whereas for SeNbS, the Janus E-field is oriented upward. The effect of Janus field orientation was previously reported to, for example, directly impact the charge transfer in a Janus-TMD heterostructure. Specifically, an ultrafast charge transfer was

reported from Janus to the regular TMD layer when the current was along the direction of the Janus field.[4] Additionally, the build-up of intrinsic strain was reported in Janus structures caused by the difference in the Bohr radius between the top and bottom chalcogen atoms. The strain can be tensile in the top chalcogen atomic layer and compressive in the bottom chalcogen layer (or the other way around), which is ultimately dictated by the Janus orientation (e.g., SeWS vs. SWSe) and lays the foundation of Janus nanoscroll formation.[5]

XPS stoichiometry ratio analysis

The XPS stoichiometry ratio of NbS_2 converted SNbSe was calculated to be S:Nb:Se=1.09:1.16:1 based on the peak area ratio of S 2p, Nb 3d, and Se 3p and their respective RSF values for the Kratos Axis Supra+, using the relation

$$S{:}Nb{:}Se = \frac{A_{S\ 2p}}{RSF_{S\ 2p}}{:}\frac{A_{Nb\ 3d}}{RSF_{Nb\ 3d}}{:}\frac{A_{Se\ 3p}}{RSF_{Se\ 3p}}$$

The resulting chalcogen ratio of S:Se (1.09:1) showed an orbital agreement within 10%, consistent with previous Janus reports,[6, 7] while a slight abundance of S and Nb relative to Se was observed. Since Se is the newly introduced chalcogen in SNbSe through the SEAR selenization process, and being the lesser atomic ratio of the three, we could hypothesize that this stoichiometric imbalance may have originated from the CVD-grown NbS_2. Importantly, although the CVD-grown NbS_2 sample used for SNbSe conversion consists mostly of monolayers, a small number of bi- and tri-layer NbS_2 could have also been present within the X-ray detection spot during the characterization, which could effectively skew in the stoichiometry in S and Nb. For these reasons, the XPS elemental analysis primarily focused on detecting individual elements and confirming that the top selenium atoms are bonded to Nb, while phononic and structural characterizations through Raman and STEM were used to confirm the synthesis and phase change of the Janus structure.

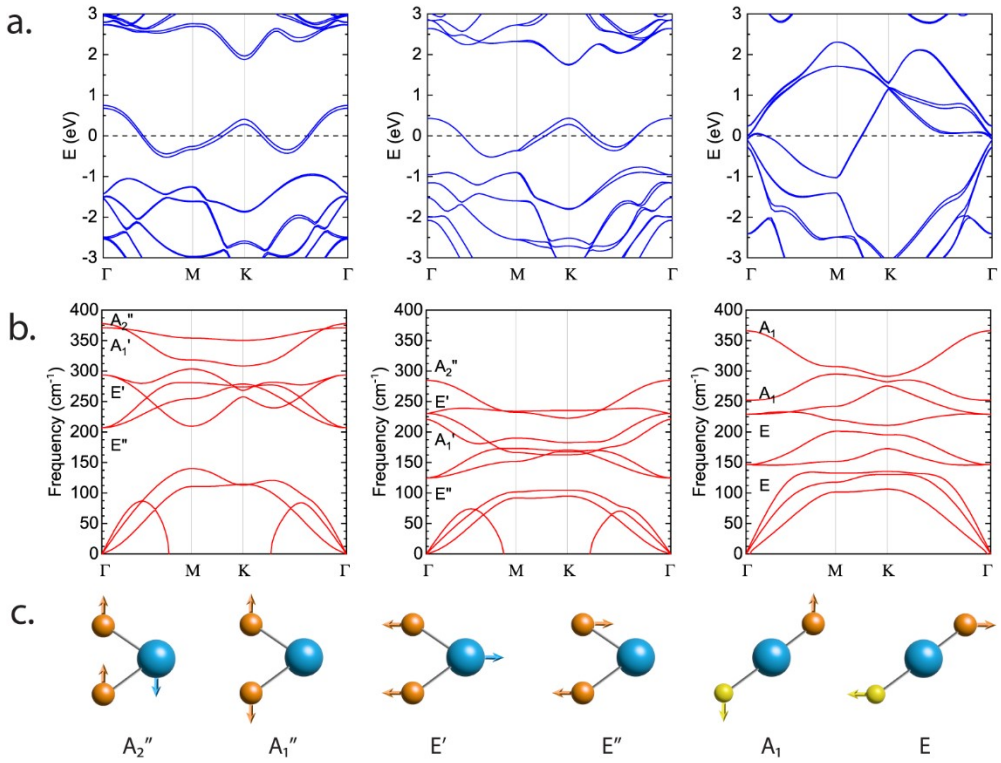

Figure S1 First principle density functional theory (DFT) calculation for (a) electronic band structure of 1H-NbS_2, 1H-$NbSe_2$, 1T-SNbSe (from left to right), (b) phonon dispersion band structure for 1H-NbS_2, 1H-$NbSe_2$, 1T-SNbSe (from left to right) and identifying different in-plane and out-of-plane vibrational modes associated with each band. Notably, imaginary modes were observed at the M and K points for NbS_2 and $NbSe_2$ as a result of instability associated with CDW phase, which have been experimentally realized.[8, 9] These instabilities are not preserved once the structure transforms to 1T phase as shown in the softening of CDW phonon mode. (c) Schematic representation of atomic vibrational modes at Γ point of the Brillouin Zone. Blue atom represents niobium, orange atom represents selenium, and the yellow atom represents sulfur atom.

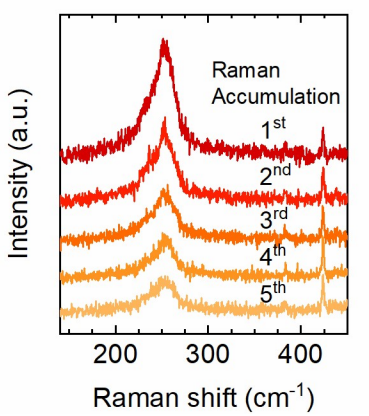

Figure S2 Stacked Raman spectrum of 5 individual accumulations in a single measurement, showing the degradation in A' mode intensity with laser exposure time. The measurement was taken with 40 second exposure time for each of the five consecutive accumulations, making it total of 200 seconds laser exposure. The decrease in A' mode intensity highlights the oxidation degradation effect.

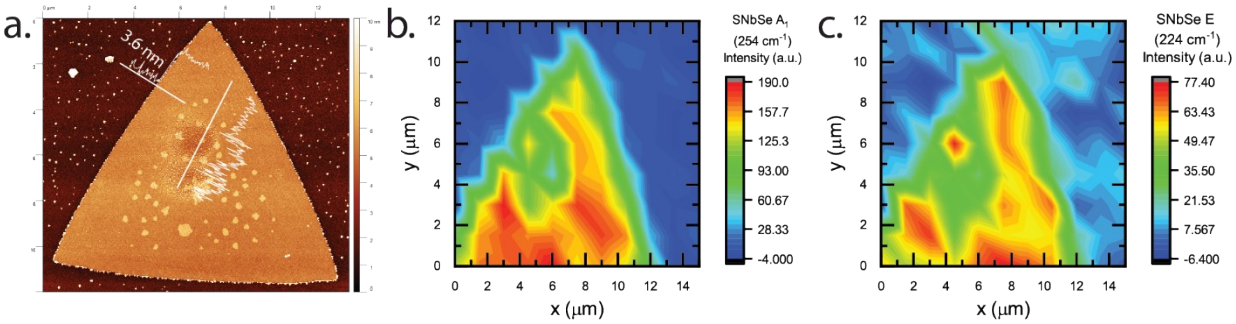

Figure S3 Laser induced degradation on the surface of SNbSe Janus converted from an APCVD grown 4-layer NbS_2 domain revealed through (a) Semi-contact mode AFM topography scan, which shows two surface indentation and roughening at the locations where single-point Raman measurements were taken using 488 nm laser with ~100 μW power (b)-(c) Raman intensity mapping at SNbSe A_1 mode (254 cm^{-1}) and E mode (224 cm^{-1}). At both frequencies, the Raman at the regions exposed to laser degradation show reduced intensity by almost half compared to the unexposed region. The edge of the triangular domain also showed lower Raman intensities, most likely due to partial laser spot coverage of the substrate.

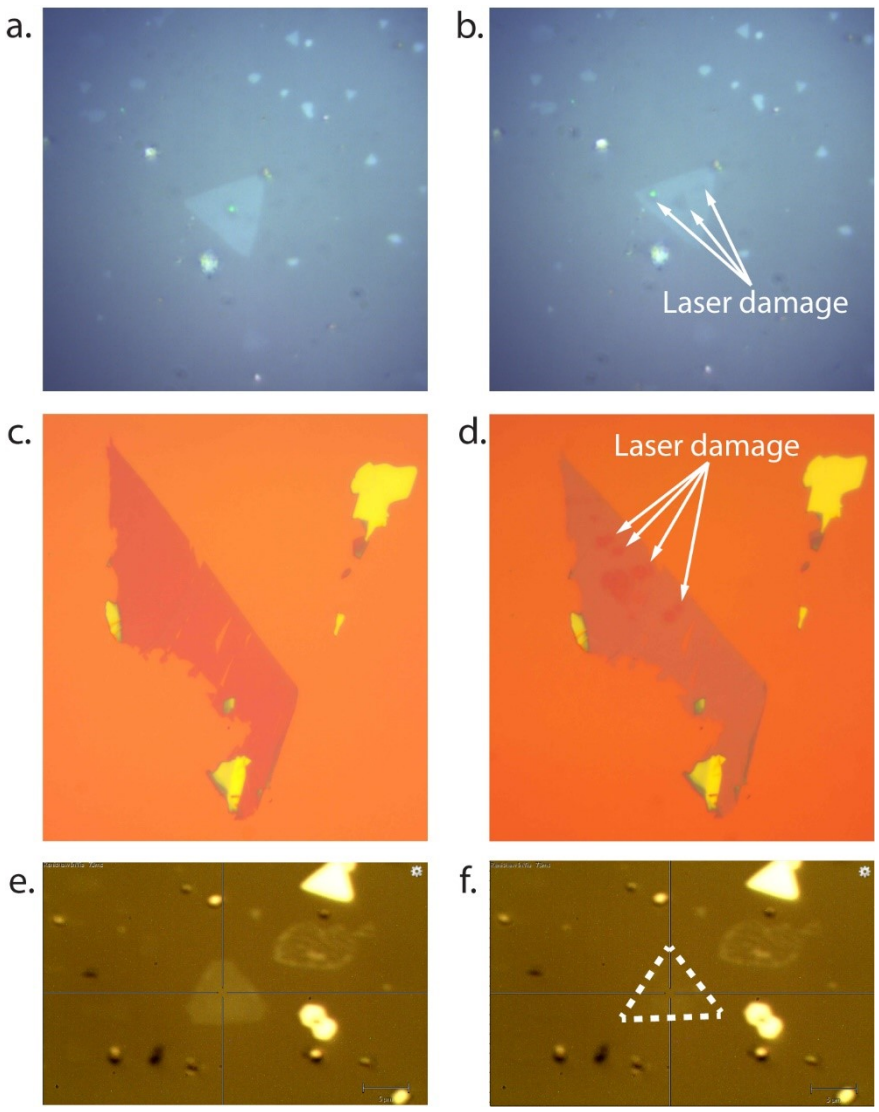

Figure S4 Laser induced degradation comparison for (a)-(b) Janus SNbSe converted from APCVD grown NbS_2 before and after laser exposure, respectively, showing multiple spot degradation after 6 mW laser exposure for 200 seconds. (c)-(d) Janus SeNbS converted from exfoliated $NbSe_2$ showing before and after laser exposure and visible degradation at multiple areas across the sample (e)-(f) Janus SNbSe converted from APCVD grown NbS_2 before and after undergoing laser rasterization at 0.2 μW for 60 second for each spot across the sample, showing large area degradation.

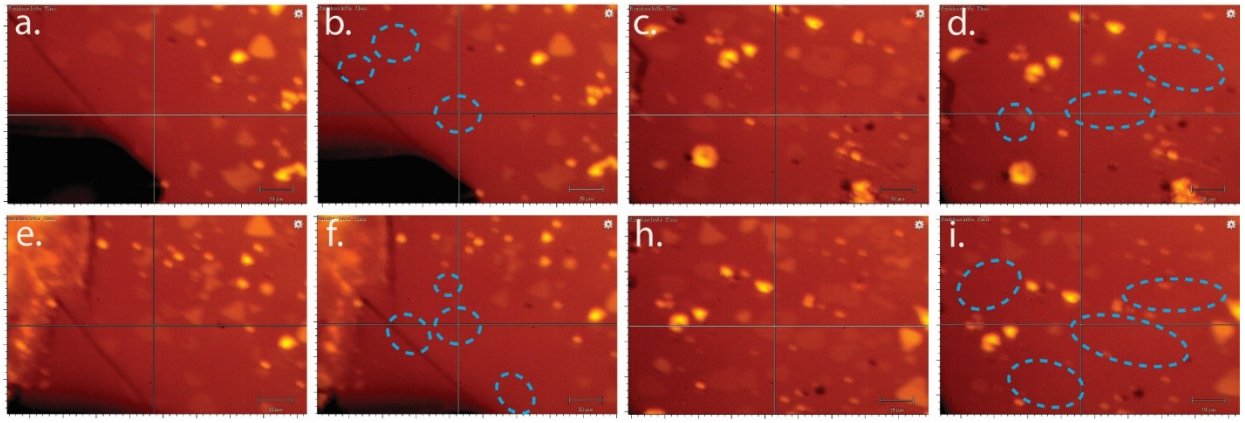

Figure S5 Monolayer SNbSe converted from APCVD-grown NbS_2 and left in ambient condition after several days, showing reduced visibility in multiple areas. Shown in (a), (c), (e), and (h) are SNbSe Janus flakes before oxidation, followed by (b), (d), (f), and (i), respectively, after oxidation.

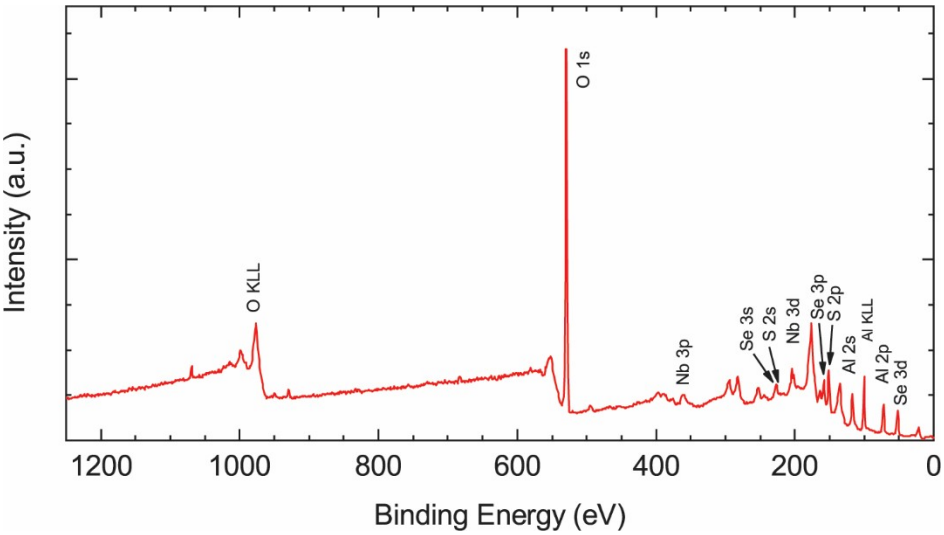

Figure S6 X-ray photoelectric spectroscopy wide survey scan of SNbSe Janus structure converted from APCVD grown monolayer NbS_2 on Al_2O_3 by SEAR selenization.

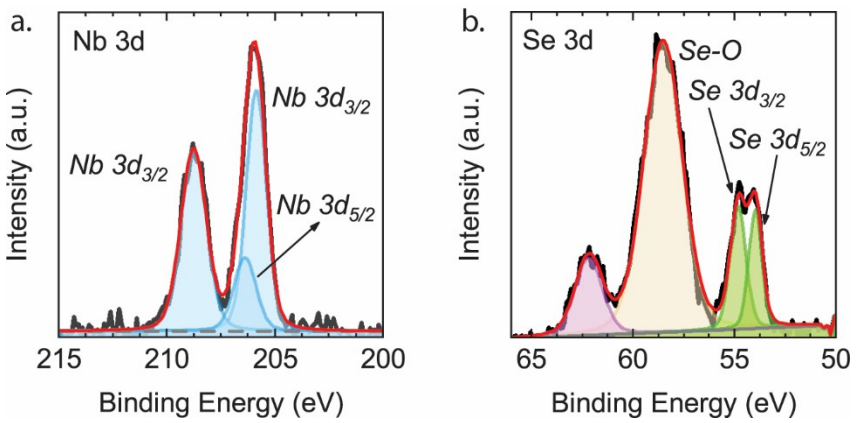

Figure S7 X-ray spectroscopy of SNbSe with oxidation characteristics indicated through (a) disappearance of Nb $3d_{5/2}$ peak and redshift of the remaining Nb peaks, which suggest the formation of Nb-O bonding and niobium-related oxide layers. (b) The emergence of a prominent Se-O peak at 59 eV, adjacent to the Se $3d_{3/2}$ and Se $3d_{5/2}$ doublet, suggests surface oxidation on the newly decorated Se atoms. An additional peak seen at 62 eV possibly originated from Nb 4s orbital of Nb_2O_5 or NbO_2 formation. This partial oxidation is likely attributed to the exposure of the top Se layer to ambient conditions.

REFERENCES

(1) Chatterjee, U.; J. Zhao; M. Iavarone; R. Di Capua; J.P. Castellan; G. Karapetrov; C.D. Malliakas; M.G. Kanatzidis; H. Claus; J.P. Ruff; F. Weber; J. van Wezel; J.C. Campuzano; R. Osborn; M. Randeria; N. Trivedi; M.R. NormanS. Rosenkranz, Emergence of coherence in the charge-density wave state of 2H-NbSe2. *Nat Commun*, **2015**. 6: p. 6313.

(2) Qin, Y.; M. Sayyad; A.R. Montblanch; M.S.G. Feuer; D. Dey; M. Blei; R. Sailus; D.M. Kara; Y. Shen; S. Yang; A.S. Botana; M. AtatureS. Tongay, Reaching the Excitonic Limit in 2D Janus Monolayers by In Situ Deterministic Growth. *Adv Mater*, **2022**. 34(6): p. e2106222.

(3) Trivedi, D.B.; G. Turgut; Y. Qin; M.Y. Sayyad; D. Hajra; M. Howell; L. Liu; S. Yang; N.H. Patoary; H. Li; M.M. Petric; M. Meyer; M. Kremser; M. Barbone; G. Soavi; A.V. Stier; K. Muller; S. Yang; I.S. Esqueda; H. Zhuang; J.J. FinleyS. Tongay, Room-Temperature Synthesis of 2D Janus Crystals and their Heterostructures. *Adv Mater*, **2020**. 32(50): p. e2006320.

(4) Zheng, T.; Y.C. Lin; N. Rafizadeh; D.B. Geohegan; Z. Ni; K. XiaoH. Zhao, Janus Monolayers for Ultrafast and Directional Charge Transfer in Transition Metal Dichalcogenide Heterostructures. *ACS Nano*, **2022**. 16(3): p. 4197-4205.

(5) Sayyad, M.; Y. Qin; J. Kopaczek; A. Gupta; N. Patoary; S. Sinha; E. Benard; A. Davis; K. Yumigeta; C.L. Wu; H. Li; S. Yang; I.S. Esqueda; A. SinghS. Tongay, Strain Anisotropy Driven Spontaneous Formation of Nanoscrolls from 2D Janus Layers. *Advanced Functional Materials*, **2023**. 33(42).

(6) Zhang, J.; S. Jia; I. Kholmanov; L. Dong; D. Er; W. Chen; H. Guo; Z. Jin; V.B. Shenoy; L. ShiJ. Lou, Janus Monolayer Transition-Metal Dichalcogenides. *ACS Nano*, **2017**. 11(8): p. 8192-8198.

(7) Lin, Y.C.; C. Liu; Y. Yu; E. Zarkadoula; M. Yoon; A.A. Puretzky; L. Liang; X. Kong; Y. Gu; A. Strasser; H.M. Meyer, 3rd; M. Lorenz; M.F. Chisholm; I.N. Ivanov; C.M. Rouleau; G. Duscher; K. XiaoD.B. Geohegan, Low Energy Implantation into Transition-Metal Dichalcogenide Monolayers to Form Janus Structures. *ACS Nano*, **2020**. 14(4): p. 3896-3906.

(8) Bianco, R.; I. Errea; L. Monacelli; M. CalandraF. Mauri, Quantum Enhancement of Charge Density Wave in NbS(2) in the Two-Dimensional Limit. *Nano Lett*, **2019**. 19(5): p. 3098-3103.

(9) Nakata, Y.; K. Sugawara; S. Ichinokura; Y. Okada; T. Hitosugi; T. Koretsune; K. Ueno; S. Hasegawa; T. TakahashiT. Sato, Anisotropic band splitting in monolayer NbSe2: implications for superconductivity and charge density wave. *npj 2D Materials and Applications*, **2018**. 2(1).